Accepted Manuscript

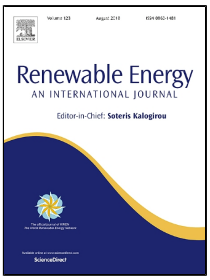

A Graphene-based Microporous Layer for Proton Exchange Membrane Fuel Cells: Characterization and Performance Comparison

Adnan Ozden, Samaneh Shahgaldi, Xianguo Li, Feridun Hamdullahpur

PII:	S0960-1481(18)30376-8
DOI:	10.1016/j.renene.2018.03.065
Reference:	RENE 9934
To appear in:	*Renewable Energy*
Received Date:	24 September 2017
Revised Date:	21 December 2017
Accepted Date:	24 March 2018

Please cite this article as: Adnan Ozden, Samaneh Shahgaldi, Xianguo Li, Feridun Hamdullahpur, A Graphene-based Microporous Layer for Proton Exchange Membrane Fuel Cells: Characterization and Performance Comparison, *Renewable Energy* (2018), doi: 10.1016/j.renene.2018.03.065

A Graphene-based Microporous Layer for Proton Exchange Membrane Fuel Cells: Characterization and Performance Comparison

Adnan Ozden[a,b], Samaneh Shahgaldi[b], Xianguo Li[a,b], Feridun Hamdullahpur[a]

[a]*Department of Mechanical and Mechatronics Engineering, University of Waterloo, 200 University Avenue West, Waterloo, ON N2L 3G1, Canada*

[b]*20/20 Laboratory for Fuel Cell and Green Energy RD&D, Department of Mechanical and Mechatronics Engineering, University of Waterloo, 200 University Avenue West, Waterloo, ON N2L 3G1, Canada*

Corresponding author: xianguo.li@uwaterloo.ca (Xianguo Li) Tel.: +1 519 888 4567

Abstract

Water management is a critical issue for proton exchange membrane (PEM) fuel cells, and the use of a microporous layer (MPL) substantially improves the PEM fuel cell performance, reliability and durability through improved water management. In this study, graphene, technically a yet-to-be-developed category of material, is investigated as a potential MPL material, due to its high electrical and thermal conductivity. MPLs made of graphene (G-MPL) have been fabricated and assessed through morphological, microstructural, physical, and electrochemical characterizations and performance testing in a single scaled-up cell. Comparison is also made with MPLs made of a conventional material, Vulcan (V-MPL). The results show that the G-MPL has a unique morphology composed of horizontally packaged graphene flakes that improves water management, in-plane electrical conductivity (up to 2 times), catalyst activity, and platinum (Pt) utilization (up to 10%). The cell with the G-MPL has a better performance than the cell with the V-MPL under both fully (100% RH) and partially (40% RH) humidified conditions, with the peak power densities of 0.98 W cm^{-2} and 0.60 W cm^{-2}, respectively – these peak power densities are about 7% and 43% higher than those obtained for the cell with the V-MPL at 100% and 40% RH, respectively.

Keywords: Proton exchange membrane fuel cell; Water management; Gas diffusion layer; Microporous Layer; Graphene-based microporous layer

1. Introduction

Proton exchange membrane (PEM) fuel cell is a promising electrochemical device that efficiently converts the chemical energy of hydrogen and oxygen into electricity through electrochemical reactions and produces only water and heat as the by-products [1–4]. A PEM fuel cell system is generally equipped with an external humidifier to ensure a desirable humidification level for the membrane-electrode assembly (MEA). However, such a method of humidification not only reduces the overall efficiency (by triggering parasitic power

consumption) but also increases the cost, weight, and complexity of the system [5]. If a sufficient level of humidification could be maintained without an external humidifier, then the overall system cost could be greatly diminished, which would conclusively advance the commercial viability of the PEM fuel cell technology. An effective strategy towards accomplishing this target is to propose a well-engineered MEA design that can retain sufficient water for effective humidification without the need of an external humidifier under a wide range of operating conditions [6]. Thus, it is pressing to develop effective design methodologies and innovative materials for the microporous layer (MPL), a critical constituent that plays a critical role in water management [7].

The MPL, typically contains a carbon-based powder and a hydrophobic agent, is deposited simply onto the gas diffusion layer (GDL) as a thin layer; accordingly, it takes up only a small fraction of GDL thickness. Thus far, numerous carbon-based commercial products – ranging from Vulcan® XC-72R [8], Ketjenblack® EC-300J [9], Ketjenblack® EC-600JD [10], to Black Pearls® 2000 [11] and Hicon Black® [7] – have been considered as a potential material for MPLs, since they are an excellent combination of favorable characteristics, such as high thermal and electrical conductivity, favorable structural and surface characteristics, wide availability, and economical viability [12]. However, by their very nature, these carbon-based nanomaterials are susceptible to oxidation when they are exposed to a highly oxidative environment during PEM fuel cell operation, restricting their applicability – for instance, long-term functionality, alongside suboptimal thermo-chemical stability [13]. Besides these "bottlenecks", the MPLs made of these materials only perform properly (without any performance compromise) under a very limited range of operating conditions (see, [6,14] for example), a challenge to their potential use for next-generation MPLs.

Recently, graphene, a two-dimensional (2D) building block for carbon materials with all other dimensionalities (as illustrated in Fig. 1) [15], has emerged as an alternative to conventional carbon-based materials in numerious fields of energy and environmental studies (see, [16,17] for instance) – primarily motivated by its unsurpassed characteristics – for example, excellent electrical and thermal conductivity, along with exceptional mechanical stiffness and elasticity [18] – characteristics that may also spark exponentially growing interests in graphene's potential as an alternative MPL material. However, until now, despite graphene's wide range of applications and distinctive characteristics, there have been only two studies investigating its potential use for MPL preparation in the open literature. Table 1 summarizes the motivation and content of these studies. As seen from Table 1, Leeuwner et al. [19] have

assessed commercial graphene foam as a free-standing layer in a small-scale PEM fuel cell (with an electrode geometric area of 5 cm^2) and claimed that situating the graphene foam provides a spectrum of benefits by improving mechanical integrity between the catalyst layer and GDL, reducing interfacial electrical resistance, and ensuring an improved water management, specifically at low- and intermediate current densities. More recently, Najafabadi et al. [18] have assessed the performance of the MPLs made of ultrathin graphene sheets for small-scale PEM fuel cells and reported their performance-enhancing effects, specifically under low-humidity conditions.

These studies have provided an excellent background for further studies by revealing positive effects of graphene-based MPLs, particularly under low-humidity conditions, along with several open questions that require further investigation. For example, the morphological, microstructural, physical, and electrochemical characteristics of graphene-based MPLs have not been fully understood yet. Equally important, the performance characteristics of graphene-based MPLs in scaled-up PEM fuel cells have not been studied or at least not reported so far. Thus, these investigations as reported in this study will significantly contribute to finding an answer to the pertinent question of will the introduction of graphene into MPLs can break the PEM fuel cells' dependence on external humidifiers for membrane humidification, or will next-generation PEM fuel cells be assembled with graphene-based MPLs. The objective of the present study is therefore to address these open questions by assessing graphene-based MPL's morphological, physical and structural characteristics, scrutinizing its performance in a scaled-up cell (with an electrode geometric area of 45 cm^2), and investigating its potential influences on catalyst activity, platinum (Pt) utilization, and ohmic resistance (Table 1).

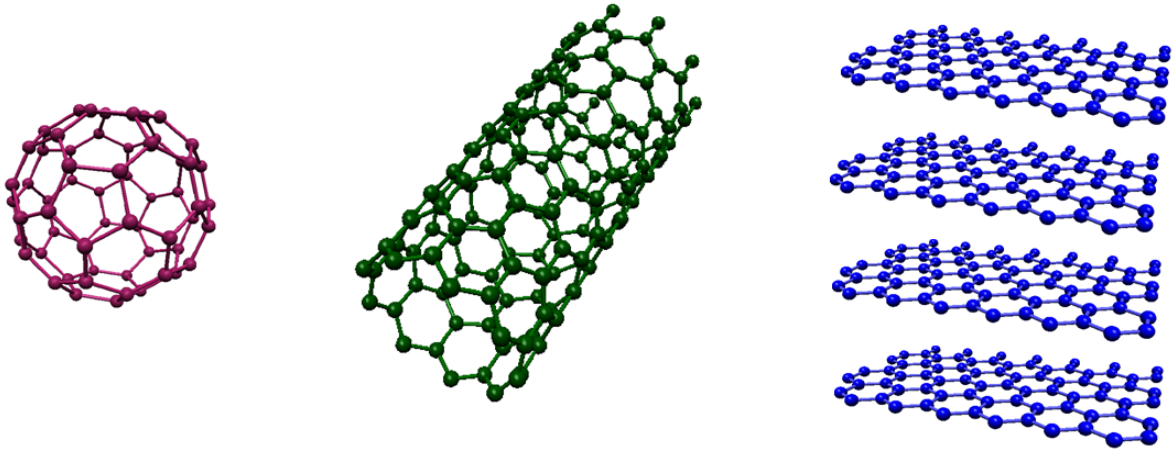

(a) **(b)** **(c)**

Fig. 1. Illustrations of (a) wrapping up of graphene into a zero-dimensional (0D) buckyball, (b) rolling of graphene into a one-dimensional (1D) nanotube, and (c) stacking of graphene into three-dimensional (3D) graphite, as adopted from [15].

Table 1. Summary of the relevant studies focusing on the investigation of graphene as an alternative MPL material.

Reference	Motivation	MPL material	MPL properties	MPL characterization	Fuel cell type
Leeuwner et al. [19]	Investigate the interfacial interactions between the catalyst layer and graphene foam	Commercial graphene foam	– Inserted into the membrane electrode assembly (MEA) as a free-standing layer – Employed on the cathode side – No hydrophobic treatment – Thickness – 30-50 µm – Porosity – 20-40%* – Pore size – 30-200^{+} µm	– Surface morphology and roughness – Wettability – Through-plane electrical resistance – In-plane resistivity and interfacial contact resistance – Interfacial contact area	Small-scale cell with an electrode geometric area of 5 cm^2
Najafabadi et al. [18]	Evaluate the electrochemically produced graphene micro-sheets as MPLs	Electrochemically produced graphene	– Fabricated with spray-coating – Employed on the cathode side – Hydrophobic treatment – 20 wt.% PTFE – Material coating – 1.5 mg cm^{-2} – Thickness – 20-30 µm – Porosity – 30-40%	– Surface morphology – Wettability – Kinetic and mass transport properties (exchange current density, through-plane gas permeability, porosity, and through-plane water permeability)	Small-scale cell with an electrode geometric area of 5 cm^2
Present study	Investigate the practical viability of graphene-based MPLs for scaled-up fuel cells	Graphene powder (heXo-G V20)	– Fabricated with spray-coating – Employed on the cathode side – Hydrophobic treatment – 20 wt.% PTFE – Material loading – 2.0 mg cm^{-2} – Thickness – 22-26 µm – Porosity – 58.8%	– Surface morphology – Microstructural analyses (porosity, pore size distribution, mean pore size, total pore volume, and bulk density) – Physical analyses (in-plane electrical resistivity, through-plane air permeability, and wettability) – Electrochemical analyses (cyclic voltammetry and electrochemical impedance spectroscopy)	Scaled-up cell with an electrode geometric area of 45 cm^2

* denotes the specifications provided by the manufacturer
$^{+}$ denotes the specification obtained from imaging

2. Experimental

2.1. *Microporous layer (MPL) fabrication*

To fabricate the MPLs made of either graphene (heXo-G V20, NanoXplore, specific (BET) surface area: 30 m^2 g^{-1}) (G-MPL) or Vulcan (Vulcan® XC-72R, Fuel Cell Store, specific (BET) surface area: 220 m^2 g^{-1}) (V-MPL), a similar procedure involving successive steps are followed. However, for brevity, in this section, only the one followed for the fabrication of the G-MPL is described. Firstly, a slurry is prepared by sequentially adding graphene powder, isopropyl alcohol (99.9%, IPA, Sigma Aldrich®), deionized (DI) water, and polytetrafluoroethylene (PTFE, 60 wt.%, Sigma Aldrich®) to a glass vessel. Secondly, the resulting slurry is mechanically stirred by an ultrasonic bath (Fischer Scientific™, 5800) at room temperature for 2 h. Thirdly, the single-layer GDL (Avcarb EP40 carbon paper) is subjected to a pressurized nitrogen gas to sweep away any contaminants embedded in it, followed by spray-deposition of the slurry onto only one surface of the single-layer GDL and heat treatment at 240°C for 1 h to evaporate any remaining moisture. Lastly, the fully dried now dual-layer GDL is sintered at 350°C for 40 min to ensure a well proportioned PTFE distribution throughout the surface. The loadings of the employed powder (graphene or Vulcan) and PTFE for both the MPLs are kept identical as 2.0 mg cm^{-2} and 20 wt.%, respectively, as recommended in [20].

2.2. *Membrane electrode assembly (MEA) fabrication*

Prior to fabrication of the MEAs, the catalyst slurry, which contains carbon-supported platinum (Pt/C, 68 wt.%), isopropyl alcohol, 25 wt.% perfluorosulfonic acid, and deionized (DI) water, is prepared and spread directly onto the both sides of the membrane (Nafion® 211) until the anode and cathode catalyst loadings of 0.1 and 0.4 mg cm^{-2}, respectively, are achieved. Thereafter, the sample of interest dual-layer GDL (the dual-layer GDL either with the G-MPL or V-MPL) is placed on the cathode side, while the commercially available dual-layer GDL (Avcarb GDS3250) is employed on the anode side.

2.3. *Characterization of dual-layer GDLs*

2.3.1. *Morphological, microstructural and physical characterization*

The morphologies of the single- (without MPL) and dual-layer (after MPL deposition) GDLs are examined via a scanning electron microscope (Zeiss GeminiSEM 300). Scanning electron microscopy (SEM) images are purposefully captured from both the top and cross-sectional

views to obtain information about the samples' surface and cross-sectional characteristics. All of the presented images are recorded from the samples without gold coating.

The pore characteristics of the single- and dual-layer GDLs are assessed by following a procedure, similar to that reported by Zamel and Li [21], via an automated standard porosimeter (Porotech Standard Porosimeter, 3.1). In its simplest form, this procedure relies on (i) evacuating the air inside the test sample cut into a circular shape (23 mm in diameter), (ii) soaking the test sample into octane (>99%, anhydrous, Sigma Aldrich®), along with two standard samples, (iii) weighing the samples before and after immersing them in octane, (iv) sandwiching the test sample between the two standard samples and recording the change in the weights of the samples (due to evaporation) through consecutive measurements, and (v) generating the capillary pressure curve for the test sample by utilizing the known capillary pressure curves for the standard samples.

The electrical resistivities of the dual-layer GDLs are measured through a four-probe technique, as discussed in detail in [22], by a probe station (Cascade microtech), compatible with a four-point head (C4S). Prior to measurements, the test sample is mounted on an insulating plate, and the tungsten tips connected to the equally spaced probes are embedded in the sample. A constant voltage of 50 mV (with frequency of 1 kHz) is applied between the outer probes, and the corresponding resistance (according to the Ohm's Law) between the two inner probes is recorded. The in-plane resistivity for each sample is then determined in a manner similar to that suggested in [22]. For each sample, at least 20 measurements are conducted in 3 different orientations. The collected resistance values present a homogeneous distribution in a narrow range, whereupon the data will be presented as the range.

The through-plane air permeabilities of the dual-layer GDLs are obtained by following a procedure similar to that discussed in detail in [23] via a custom-built experimental setup. The measurements through this procedure involves (i) situating the test of interest sample cut into a circular shape (30 mm in diameter) between two metal disks, (ii) supplying air at 75°C with varying flow rates (from 500 to 100 ml/min, in 100 ml/min decrements) and recording the corresponding pressure difference across the sample, and eventually (iv) utilizing the solution of Darcy's Law for single-phase one-dimensional compressible flow through a porous medium to determine the air permeability coefficients of the samples [23]. The permeability measurements are conducted five times for each sample, and the data will be presented as the range, which captures all the permeability values determined.

Sessile drop technique is used to explore the wettability characteristics of the dual-layer GDLs by adopting a procedure, discussed in detail in [24], via a standard static contact angle goniometer (Ramé–Hart Instrument). The procedure basically involves (i) mounting a circular-shaped test sample (30 mm in diameter) on an anti-vibrating bench, (ii) dropping a water droplet with a fixed volume of 7 μl onto the sample via a dispenser, (iii) fitting a tangent line to the triple-phase point (where the droplet touches the sample surface), and (iv) determining the static contact angle via a commercial software. The measurements are carried out with three samples obtained from each test of interest dual-layer GDL, and at least 10 measurements are collected from each sample. The data are presented as a range as well, since the static contact angles obtained from the measurements present a fairly homogeneous distribution in a narrow range.

2.3.2. *Electrochemical characterization*

In-situ cyclic voltammetry (CV) and electrochemical impedance spectroscopy (EIS) analyses are performed via a computer-aided commercial fuel cell test station (Greenlight Innovation, G20), equipped with a frequency response analyzer and a booster (Gamry Instruments, 30K). CV measurements are performed under the same operating conditions for both the MEAs. In the measurements, the cathode (working electrode) and the anode (the reference and also counter electrode) of the cell are fed with humidified nitrogen and hydrogen, respectively. The voltage applied is swept from 0.10 to 0.80 V, at a scanning rate of 0.05 V s^{-1}. The cyclic voltammograms for the MEAs assembled with the dual-layer GDLs are recorded after 20 successive cycles, thereby a better accuracy is achieved for the calculated electrochemical surface areas (ECSAs) with a standard deviation of less than 2.5%. To calculate catalyst utilization, the morphology of the catalyst employed is investigated by a high-resolution transmission electron microscope (HRTEM) (Zeiss Libra® 200 MC) operated at an acceleration voltage of 200 kV. The images are recorded via a CCD camera. Samples are prepared by mixing a proper amount of catalyst with hexane in a sonicator for 30 min, followed by dropping of the resulting solution on a copper grid and drying it at room temperature.

EIS measurements are performed at 0.70 V in potentiostatic mode by applying a signal with an amplitude of 10 mA, and frequency is swept from 100 mHz to 1000 kHz. Since the reaction rate of oxygen reduction is much slower than that of hydrogen oxidation, the cell impedance is likely be dominated by the cathodic impedance [25]. Thus, the cathode electrode

is employed as the working electrode, while the anode electrode is the counter electrode (and the reference electrode as well).

2.4. *PEM fuel cell performance analysis*

The steady-state polarization characteristics of the MEAs with the dual-layer GDLs are investigated by the computer-aided commercial fuel cell test station (Greenlight Innovation, G20). The experimental setup typically consists of graphite bipolar plates with an electrode active area of 45 cm^2, along with other auxiliary equipment. On completion of leakage test, the test of interest MEA is assembled and activated. For comparison, performance testing is conducted under the same operating conditions for both the MEAs assembled either with the G-MPL or V-MPL, respectively: a cell temperature of 75°C, varied air and hydrogen relative humidities (40% RH, 70% RH, and 100% RH), an air and hydrogen back pressure of 35 kPag, and air and hydrogen flow rates of 9.00 and 4.45 l/min, respectively. To obtain the polarization curve, the current density is recorded potentiostatically from open-circuit voltage (OCV) to ~0.20 V, in 0.10 V decrements. Each polarization curve is the average of three polarization curves measured on three different days, and the standard deviation is calculated to be no more than 5%.

3. Results and Discussion

3.1. *Morphological and microstructural analyses*

The images captured from the top and cross-sectional views of the single-layer GDL (Avcarb EP40, without MPL) and the dual-layer GDLs are presented in Fig. 2. It is seen that in the single-layer GDL, the carbon fibres, as seen from Figs. 2(a) and 2(b), are oriented anisotropically along the in- and through-plane directions, which is expected to dramatically influence its physical characteristics, i.e., electrical and thermal conductivity, in these directions [26]. In addition, the single-layer GDL is abundant with macropores with sizes up to tens of micrometers (i.e., 120.2 μm, as dimensioned in Fig. 2(a)), implying that without MPL deposition, the single-layer GDL itself would not only increase the interfacial contact resistance between the GDL and catalyst layer but also deteriorate overall cell performance by allowing catalyst to penetrate deeply into GDL through the available macro-scale open pores. In the dual-layer GDL with the G-MPL, the graphene flakes with sizes up to several tens of micrometers (i.e., 27.78 μm, as dimensioned in Fig. 2(c), inset) yield fairly uniform distribution over the surface, along with no visible PTFE agglomeration and surface cracks. The graphene flakes tend to stack horizontally (i.e., in the in-plane direction) and constitute an interconnected network along the in- and through-plane directions (see Figs. 2(c) and 2(d)).

These flakes are also inclined to penetrate deeply into the GDL (see Fig. 2(d)), rather than simply accumulate in the regions on the surface or near the surface, making the MPL thickness relatively smaller (see Table 2). As a matter of fact, formation of such a composite-like dual-layer GDL structure is expected to make the physical characteristics, i.e., electrical and thermal conductivity, more uniform along the in- and through-plane directions. The dual-layer GDL with the V-MPL exhibits compact and porous surface characteristics (see Fig. 2(e), inset), but along with small amount of PTFE/Vulcan agglomeration and visible macro-scale surface cracks (see Fig. 2(e)), akin to desiccation cracks in soil. The compact structure and macro-scale surface cracks could be ascribed to the fairly small average particle size of Vulcan, typically around 40 nm [27]. Similar to the G-MPL, the V-MPL is not simply deposited onto the single-layer GDL but, rather, penetrates deeply into it (see Fig. 2(f)), which is also expected to make the physical characteristics similar along the in- and through-plane directions. This penetration could also be a contributing factor to the relatively small MPL thickness (see Table 2).

The pore characteristics of the single- and dual-layer GDLs are determined through a series of porosimetry analyses, as presented in Fig. 3 and Table 2. For the sake of comparison and also to simplify the classification of microstructural characteristics, the pores within the GDLs under consideration are identified according to their size: the pores smaller than 0.07 μm are identified as micropores, the pores in the range of 0.07-5 μm are as mesopores, and the pores larger than 5 μm are as macropores. For the single-layer GDL, about 6.6% of the cumulative pore volume is taken up by the micropores, while approximately 41.6% and 51.8% of that is taken up by the mesopores and macropores, respectively. The relatively less micro-pore volume within the single-layer GDL is ascribed to the small PTFE agglomerates, whereas a relatively higher volume of meso- and macropores could be related to the interconnected network formed by carbon fibers, which may also be corroborated by the SEM observation of the single-layer GDL (see Fig. 2(a)). For the dual-layer GDL with the G-MPL, approximately 11.1% of the cumulative pore volume is taken up by the micropores, whereas 69.3% and 19.6% of that is taken up by the mesopores and macropores, respectively. It is clear that deposition of the G-MPL leads to formation of more micro- and mesopores (since the micro- and meso-pore volumes increase from 6.6% to 11.1% and 41.6% to 69.3%, respectively), whereas gives rise to a noticeable decrease in the volume of macropores (from 51.8% to 19.6%). The increase in the volume of micro- and mesopores is likely caused by the micro-scale spaces at the interfaces of graphene flakes/PTFE/carbon fibers, while the reduced

macro-pore volume is a clear indication that the majority of the macro-scale pores are filled by the graphene flakes, consistent with the captured SEM images (see Figs. 2(c) and 2(d)).

For the dual-layer GDL with the V-MPL, approximately 33.9% of the cumulative pore volume is in the micro-pore range, 38.4% is in the meso-pore range, and 27.7% is in the macro-pore range (see Fig. 3). It is clear that deposition of the V-MPL substantially increases the volume of micropores (from 6.6% to 33.9%), whereas decreases that of meso- and macropores (from 41.6% to 38.4% and 51.8% to 27.7%, respectively), potentially associated with the spherical and a relatively small average particle size of Vulcan, around 40 nm [27]. The smaller particle size of the employed powder seems to facilitate the formation of micropores, because relatively less micro-pore volume formation is observed, when graphene with a nominal particle size of 30 μm is employed, rather than Vulcan. This finding correlates well with the fairly small mean pore size (40.6 nm) of the dual-layer GDL with the V-MPL, compared to that of one with the G-MPL (179.7 nm) (see Table 2). It is also seen that deposition of the G-MPL onto the single-layer GDL only slightly reduces its mean pore size (from 190.5 to 179.7 nm), likely originating from the formation of less micropores. Lastly, as seen in Table 2, deposition of either the G-MPL or V-MPL onto the single-layer GDL leads to a perceivable decrease in its porosity, along with a slight increase in its total pore volume.

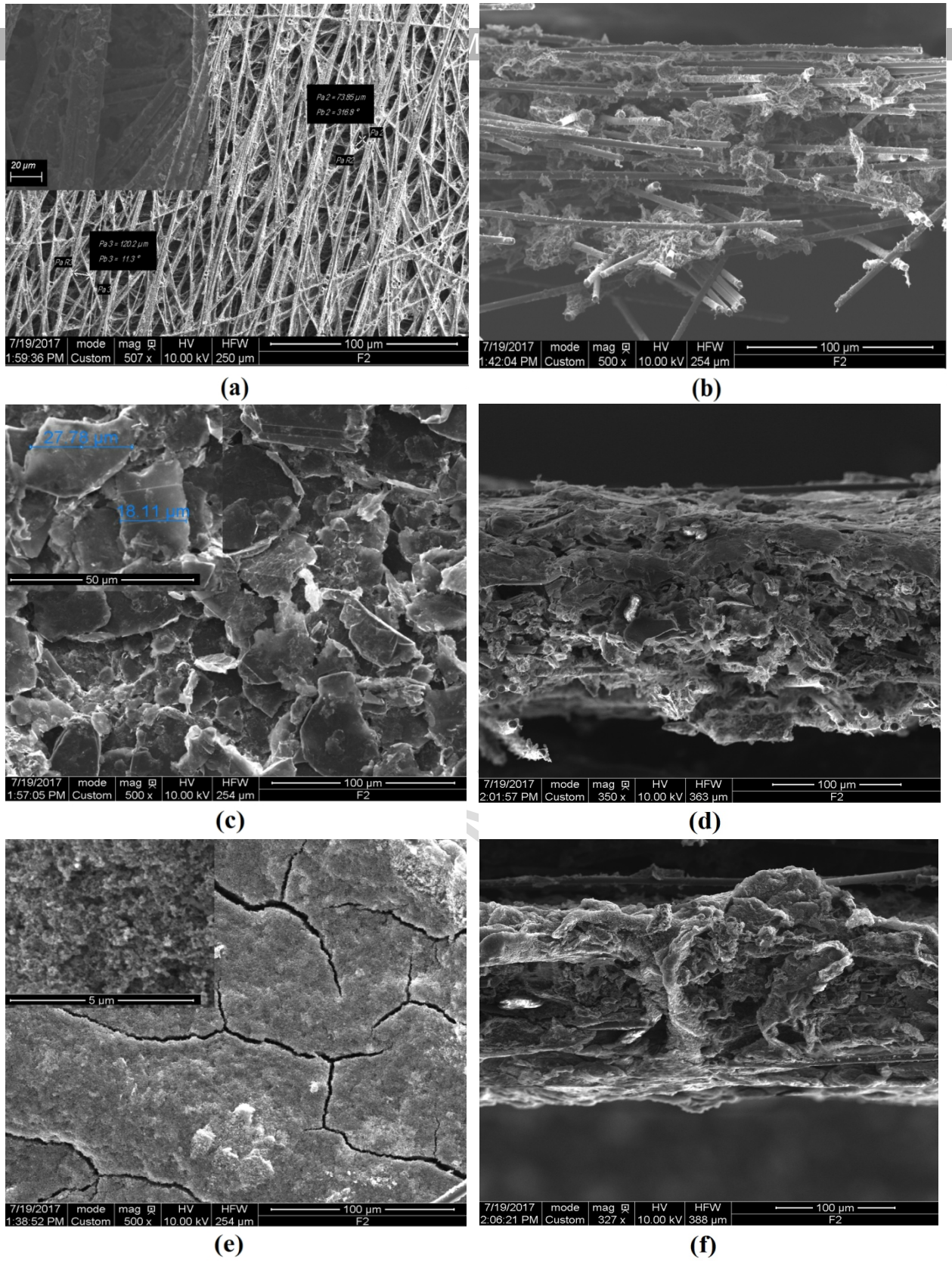

Fig. 2. SEM images of the dual-layer GDLs: (a) surface of the single-layer GDL (Avcarb EP40, without MPL), inset showing the detail of anisotropically oriented carbon fibers and macropores; (b) cross-sectional images of the single-layer GDL (Avcarb EP40, without MPL); (c) surface of the dual-layer GDL with the G-MPL, inset showing the graphene flakes with their size; (d) cross-sectional images of the dual-layer GDL with the G-MPL; (e) surface of the dual-layer GDL with the V-MPL, inset showing the porous surface characteristics,

together with small amount of Vulcan/PTFE agglomeration; (f) cross-sectional images of the dual-layer GDL with the V-MPL.

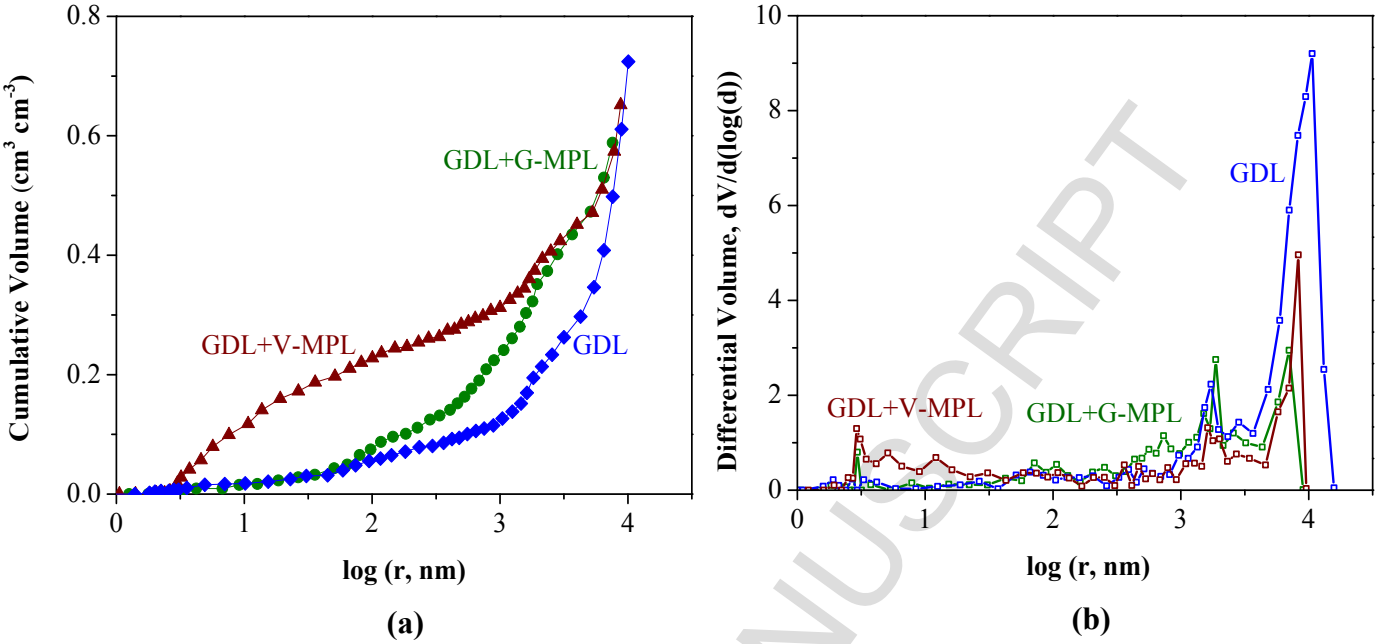

Fig. 3. (a) Cumulative and (b) differential pore size distributions in a single-layer GDL (Avcarb EP40, without MPL) and dual-layer GDLs either with the G-MPL or V-MPL. r is the pore radius; d is the pore diameter.

Table 2. Pore characteristics of the single- and dual-layer GDLs.

GDL type	MPL carbon powder type	MPL carbon loading (mg cm^{-2})	MPL PTFE content (%)	MPL thickness (μm)	Bulk density (g cm^{-3})	Porosity (%)	Mean pore size (nm)	Total pore volume (cm^3)*
Avcarb EP40	---	0	0	0	0.2212	73.8	190.5	0.0996
Avcarb EP40	Graphene heXo-G V20	2.0	20.0	22-26	0.2921	58.8	179.7	0.1023
Avcarb EP40	Vulcan XC-72R	2.0	20.0	26-30	0.3111	65.3	40.6	0.1121

*Total pore volume value is obtained from the two pieces of sample.

3.2. *Physical analyses*

A summary of the physical characteristics, i.e., in-plane electrical resistivity, through-plane air permeability and wettability, determined for the dual-layer GDLs either with the G-MPL or V-MPL is presented in Table 3.

The in-plane electrical resistivities of the dual-layer GDLs are determined according to the method of four-probe, as presented in Table 3. Since all the materials, except for the powders employed for the MPL fabrication, are the same, and the MPLs are prepared by following the

same procedure, with the matched engineering parameters, the obtained electrical resistivities for the dual-layer GDLs are expected to be a strong function of the employed powders' (graphene or Vulcan) intrinsic properties as well as the achieved electron transport capabilities when the individual particles of these powders are bound to each other by a polymeric binder [28]. Owing to its distinctive electronic structure, graphene's single-particle conductivity is exceptionally high (~10^8 S m^{-1}), while when its particles are interconnected to each other as the bulk powder (as in the case of MPL), it experiences a steepest decline (up to six orders of magnitude) in overall electron conductivity [28]. Even though graphene experiences such a dramatic drop in its electrical conductivity capability, the in-plane electrical resistivity (16.8-19.9 mΩ cm) obtained for the dual-layer GDL with the G-MPL is nearly half that of the dual-layer GDL with the V-MPL (25.3-29.7 mΩ cm), suggesting that the former provides more direct and less resistive pathways through which electrons can easily transport. Formation of such pathways may be due to the well-connected network built up by the densely packaged graphene flakes (see Fig. 2(c)).

The through-plane air permeability of a dual-layer GDL is greatly affected by its microstructural and dimensional characteristics, such as porosity, pore size distribution, mean pore size, and thickness. For instance, an increase in the porosity, mean pore size, and macro-pore volume facilitates the air transport across the sample, thereby improving its permeability, whereas an increase in the sample thickness results in a substantial drop in its permeability by increasing the complexity of the diffusion paths [29]. As evident from Table 3, compared with the dual-layer GDL with the V-MPL ((1.31-1.68) x 10^{-13}), a relatively low through-plane air permeability is obtained for the one with the G-MPL ((6.95-7.98) x 10^{-14}), which is in good agreement with the microstructural characteristics obtained for the dual-layer GDLs. As seen in Table 2, the porosity of the dual-layer GDL with the G-MPL (58.8%) is distinctly lower, compared to that of the one with the V-MPL (65.3%). Similarly, the former one has a relatively low macro-pore volume (19.6%), compared to the latter (27.7%), which is a clear sign of the presence of more resistance to the air flow. The morphological characteristics achieved upon deposition of the MPLs are also of paramount importance, particularly because they significantly influence the complexity (or tortuosity) of the air pathways. For example, the horizontally and firmly packaged macro-scale graphene flakes existing in the G-MPL probably stimulates the occurrence of a significant resistance to the air that flows in the direction perpendicular to them (see Fig. 2(c)), whereas the surface cracks (up to 15 μm wide)

on the surface of the V-MPL likely facilitates the air transport by forming more direct (or less tortuous) pathways (see Fig. 2(e)).

The wettability characteristics of the dual-layer GDLs are also investigated by determining their static contact angles. As shown in Table 3, a slightly higher static contact angle (156-160°) (a more hydrophobic characteristic) is obtained for the dual-layer GDL with the V-MPL, compared to the dual-layer GDL based on the G-MPL (152-156°), potentially ascribed to the former's slightly higher capillarity. According to the Young-Laplace equation, the capillarity of a dual-layer GDL depends to a large extent on the volume of micropores; that is, the larger the volume of micropores, the more capillary it is (see, [30] for example). Since the former's micro-pore volume (33.9%) is relatively higher than that of the latter (11.1%), its capillarity could reasonably be slightly higher. The morphology and surface characteristics (i.e., homogeneity and roughness) of the dual-layer GDLs also substantially influence the static contact angle range obtained; as such, a relatively broader range is usually detected for rough and non-uniform surfaces, because the wettability characteristics vary perceivably depending on the location of the water droplets. However, in this study, no significant location-dependent static contact angle variation is detected (see Table 3), which could, in turn, be an indication of homogeneous wettability characteristics.

Table 3. Physical characteristics of the dual-layer GDLs.

Compositions of the dual-layer GDLs							
GDL type	MPL carbon powder type	MPL carbon loading (mg cm^{-2})	MPL PTFE content (%)	MPL thickness (μm)	Static contact angle (°)	In-plane electrical resistivity (mΩ cm)	Through-plane air permeability (m^2)
Avcarb EP40	Graphene heXo-G V20	2.0	20.0	22-26	152-156°	16.8-19.9	(6.95-7.98) x 10^{-14}
Avcarb EP40	Vulcan XC-72R	2.0	20.0	24-28	156-160°	25.3-29.7	(1.31-1.68) x 10^{-13}

3.3. *Electrochemical analyses*

The cyclic voltammograms for hydrogen adsorption and desorption of the MEAs assembled either with the G-MPL or V-MPL are presented in Fig. 4. The electrochemical surface areas (ECSAs) are calculated considering the coulombic charge for hydrogen adsorption and desorption, as follows [31]:

$$\mathrm{ECSA} = \frac{\mathrm{Q_{Pt}}}{\mathrm{Q_{ref} m_{Pt}}} \quad (1)$$

where Q_{Pt} and Q_{ref} are the total charge of the hydrogen adsorption/desorption area and adequate charge for oxidizing a monolayer of hydrogen on the platinum (Pt) surface, respectively, and m_{Pt} stands for the Pt loading on the electrode. It is clear that both the MEAs present the common voltammograms for hydrogen adsorption and desorption on Pt surface. However, the ECSAs calculated for the MEAs with the G-MPL and V-MPL are 87 and 79 m^2 g^{-1}, respectively; clearly the ECSA for the former is noticeably higher than that for the latter. Since the method of catalyst-coated membrane (CCM) is applied in the fabrication of both the MEAs, the effect of catalyst penetration into the dual-layer GDLs may be assumed to be negligible and cannot explain the noticeable difference between the ECSAs. The potential reasons for the higher ECSA calculated for the MEA assembled with the G-MPL could be relatively faster electron transport and a higher degree of surface contact between the G-MPL and catalyst layer. As mentioned earlier, the electrical conductivity of G-MPL is about twice that of the V-MPL; potentially accelerating hydrogen desorption reaction by providing comparatively faster electron transport. The G-MPL also presents a fairly uniform and unique morphology, in which graphene flakes are horizontally and firmly packaged (see Fig. 2(c)), probably offering a smooth layer (thus a relatively higher degree of surface contact), improving catalyst activity.

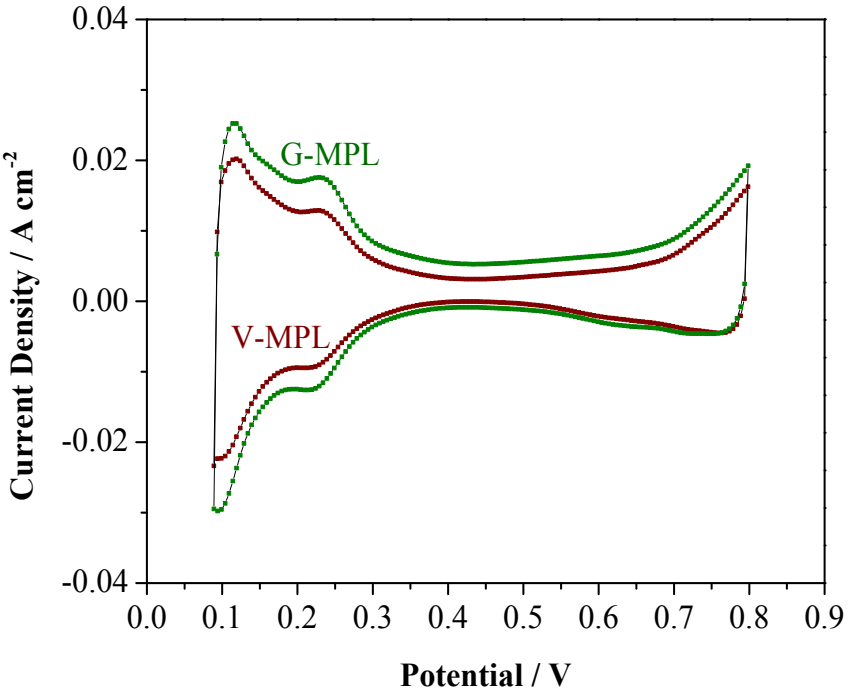

Fig. 4. Cyclic voltammograms for the MEAs assembled either with the G-MPL or V-MPL.

Pt utilization is also calculated to understand the potential impact of the employed MPL on catalyst utilization by using the cyclic voltammetry data and the size of the Pt nanoparticles. Figure 5 shows the HRTEM image of the Pt nanoparticles employed in the electrodes of both the MEAs. The surface averaged particle size (d_s) of the Pt nanoparticles is calculated in a manner similar to that reported in [32] using the following equation:

$$d_s = \sum_{i=1}^{n} n_i d_i^{\,3} \Big/ \sum_{i=1}^{n} n_i d_i^{\,2} \qquad (2)$$

where n_i represents the number of particles with a diameter of d_i. The d_s is determined by selecting at least 50 different particles from randomly captured regions, which is 2.95 nm. Pt utilization for the each MEA is estimated from the ratio of the ECSA over the geometric surface area (GSA) of the Pt nanoparticles, as follows [31]:

$$\text{Pt utilization } (\%) = \frac{\text{ECSA } (m^2/g_{Pt})}{\text{GSA } (m^2/g_{Pt})} \text{x } 100 \qquad (3)$$

The GSA of the Pt nanoparticles can be calculated by utilizing the previously determined d_s (2.95 nm) and the density of Pt (21.4 x 10^6 g m^{-3}) [33]:

$$\text{GSA}\left(m^2/g_{Pt}\right) = \frac{6}{\rho_{Pt} d_s} \qquad (4)$$

From Eqs. (1) and (4), it is found that the Pt utilization for the G-MPL and V-MPL are around 91% and 83%, respectively; suggesting clearly that the characteristics of the MPL employed has a substantial impact on catalyst activity and Pt utilization.

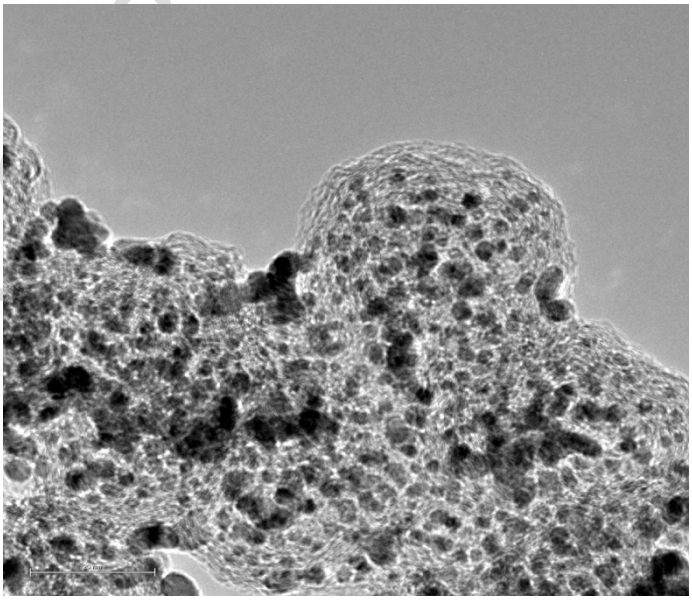

Fig. 5. HRTEM image of the Pt nanoparticles incorporated into the electrodes of the MEAs assembled either with the G-MPL or V-MPL.

Electrochemical impedance spectroscopy (EIS) is used to further examine the influence of MPL composition on the cell performance under various relative humidity (RH) conditions for the air and hydrogen streams. Figure 6 shows the impedance spectra at a cell voltage of 0.70 V as a function of air and hydrogen RHs for the PEM fuel cells assembled either with the G-MPL or V-MPL. The real (horizontal) axis intersects the impedance spectrum at the end of high-frequency arc represents the ohmic resistance. As seen from Figs. 6(a) and 6(b), the ohmic resistances increase and gradually shift to right with decreasing RHs of the air and hydrogen streams, attributable to the potential deterioration in the membranes' proton conduction capabilities, caused probably by the decrease in the water content of the membranes with the drop in the RHs of the air and hydrogen streams [34]. However, the ohmic resistance increase observed for the cell assembled with the G-MPL is relatively less, indicating clearly that the G-MPL has a greater water-retaining capability for effective membrane hydration. In each curve, the low-frequency arc represents the resistance to the transport of air to the triple-phase boundary, while the high-frequency arc is basically ascribed to the charge transfer resistance [6]. It is clear that both the high- and low-frequency arcs grow continuously with decreasing RHs of the air and hydrogen streams; however, this grow remains distinctively low for the cell assembled with the G-MPL, compared to the one based on V-MPL (see Fig. 6(c), for example), potentially related to the G-MPL's better water management and effective electron transport capability.

3.4. *Single cell performance analysis*

To provide practical insights into the water management capabilities of the G-MPL and V-MPL, PEM fuel cell performance measurements are conducted in a single and scaled-up fuel cell under the same operating conditions: a cell temperature of 75°C, an air and hydrogen back pressure of 35 kPag, air and hydrogen flow rates of 9.00 and 4.45 l/min, respectively, and varied air and hydrogen RHs (40% RH, 70% RH, and 100% RH).

Figs. 7(a) and 7(b) show the current-voltage polarization curves obtained from the MEAs assembled either with the G-MPL or V-MPL under various RHs in air and hydrogen streams. It is clearly seen that the influence of RH is quiet substantial and the cell performance depends dramatically on the humidification level of the air and hydrogen streams. Both the MEAs exhibit the best performance at the fully-humidified condition (100% RH); more specifically, the peak power densities of 0.98 W cm^{-2} and 0.92 W cm^{-2} are achieved for the

MEAs with the G-MPL and V-MPL, respectively. However, as seen from Fig. 8, when the air and hydrogen RH is decreased to 70%, their performance degrade progressively; nevertheless,

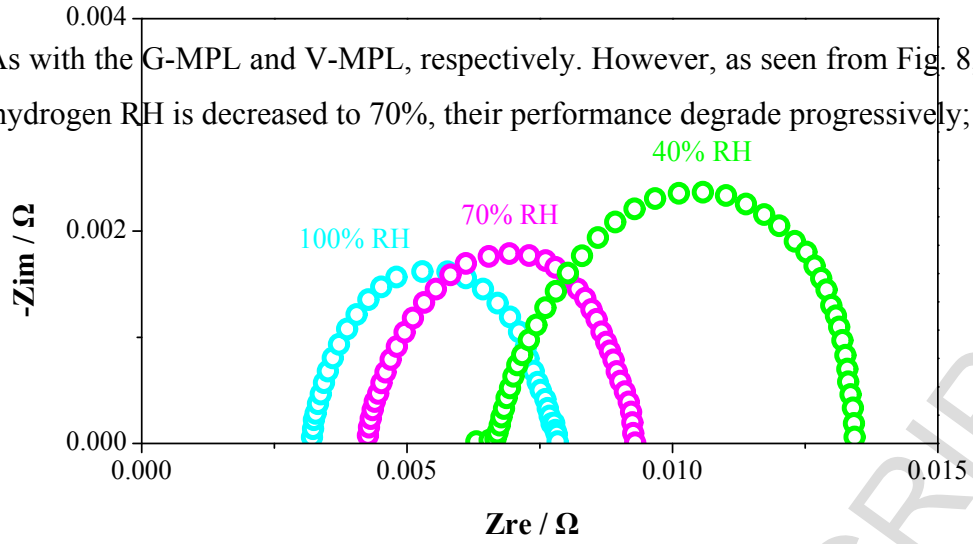

(a) with G-MPL

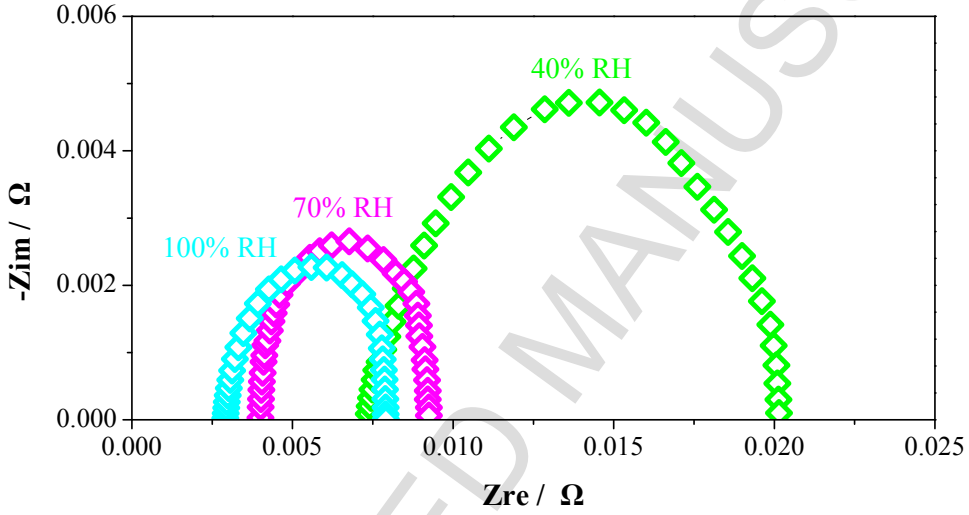

(b) with V-MPL

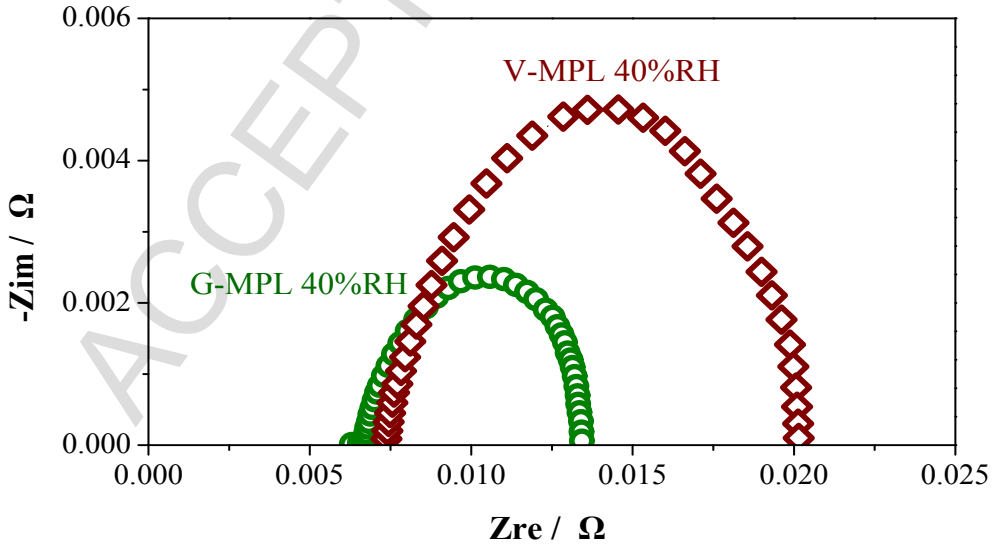

(c) comparison at 40% RH

Fig. 6. Impedance spectra for the PEM fuel cells assembled with different MPLs at 0.70 V. (a) G-MPL, (b) V-MPL, and (c) comparison at 40% relative humidity (RH). Operating temperature: 75°C, air and hydrogen back pressure: 35 kPag, varied air and hydrogen RHs (40% RH, 70% RH, and 100% RH), and air and hydrogen flow rates: 9.00 and 4.45 l/min, respectively.

the MEA with the G-MPL still shows superior performance, with a peak power density of 0.81 W cm^{-2}, compared to the one with the V-MPL (0.72 W cm^{-2}) – this corresponds to a power density superiority of about 13%. Since the similar surface-wetting characteristics (see Table 3) are observed upon deposition of both the G-MPL and V-MPL, this superior performance could be associated with the G-MPL's morphology, in which graphene flakes are firmly and horizontally stacked; potentially forming comparatively complex (more tortuous) pathways for water transport and facilitating water retention. As the air and hydrogen RH is further reduced to 40%, not surprisingly, the peak power densities for the MEAs with G-MPL and V-MPL decrease from 0.81 W cm^{-2} to 0.60 W cm^{-2} and 0.72 W cm^{-2} to 0.42 W cm^{-2}, corresponding to power density drops of about 26% and 42%, respectively. However, the peak power density of the MEA with the G-MPL is still approximately 43% higher, likely resulting from the better water management capability of the G-MPL. These findings are also in good agreement with those reported in the previous subsection for the EIS measurements. As mentioned earlier, the V-MPL has macro-scale surface cracks (up to 15 μm wide), probably forming more direct and less complex water pathways (specifically along the through- plane direction) through which the water can easily be transported by the pressure arising from membrane swelling during cell operation. Such a simplified way of water transport probably induces severe membrane dehydration under low-humidity operation (i.e., 40% RH). On basis of these findings, the application of G-MPL on the cathode side of an MEA significantly improves its performance not only under high-humidity conditions, but also low- and intermediate-humidity operation. Graphene, therefore, has not only a great promise of being widely employed as an ideal MPL material for next-generation PEM fuel cells, but also high potential for opening up an opportunity to clear away the necessity of external humidifier use for membrane hydration.

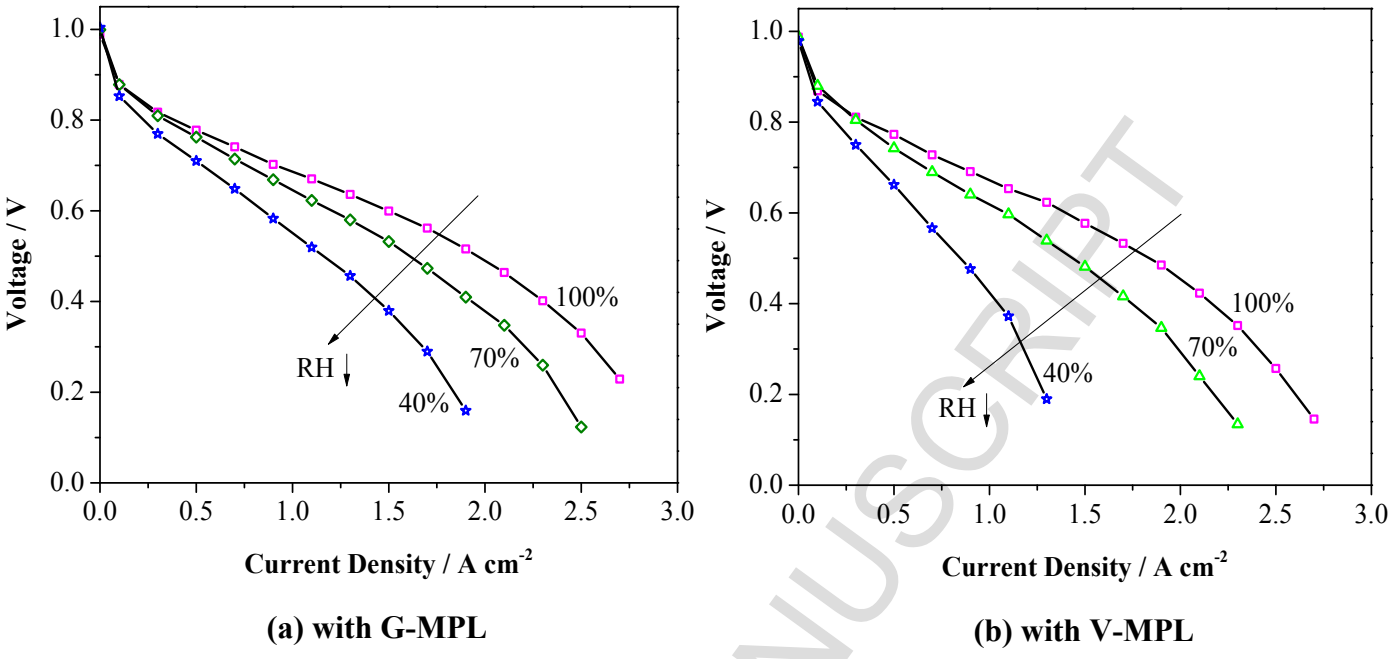

Fig. 7. Polarization curves obtained from the MEAs assembled with the (a) G-MPL and (b) V-MPL for various relative humidity (RH) conditions of the air and hydrogen streams. Operating temperature: 75°C, air and hydrogen back pressures: 35 kPag, and air and hydrogen flow rates: 9.00 and 4.45 l/min, respectively.

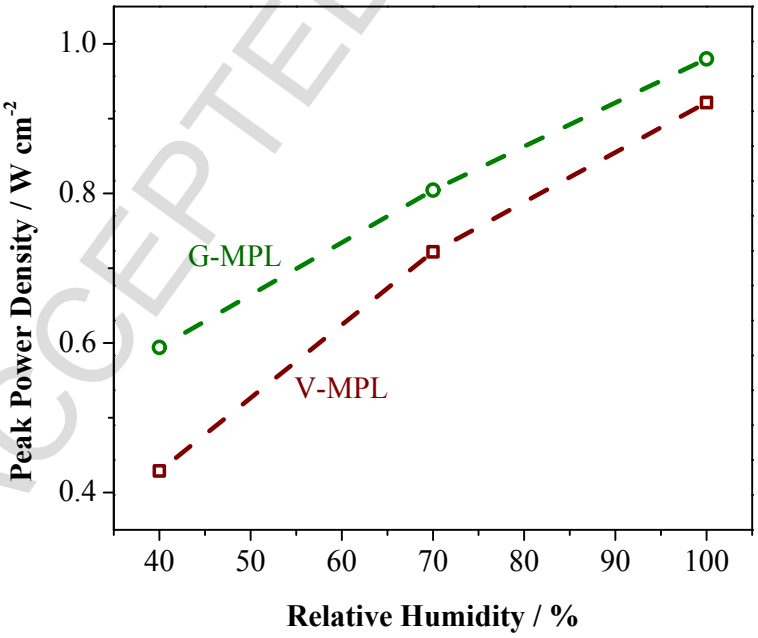

Fig. 8. Peak power densities obtained from the MEAs assembled either with the G-MPL or V-MPL for various relative humidity (RH) conditions of the air and hydrogen streams.

Operating temperature: 75°C, air and hydrogen back pressures: 35 kPag, and air and hydrogen flow rates: 9.00 and 4.45 l/min, respectively.

4. Conclusions

In this study, graphene is investigated as a potential microporous layer (MPL) material for its use in scaled-up proton exchange membrane (PEM) fuel cells. In this context, an MPL made of graphene (G-MPL) has been fabricated by the spray-deposition technique, and extensive investigation into its morphological, microstructural, physical, electrochemical characteristics, and scaled-up PEM fuel cell performance is conducted. Comparison studies are also performed with an MPL made of a widely employed MPL material, Vulcan (V-MPL). The results indicate that upon deposition of G-MPL onto the single-layer GDL, a desirable morphological structure, which not only improves electron transport and provides effective water management under both partially and fully humidified conditions, but also improves catalyst activity and platinum (Pt) utilization, has been achieved. Owing to the G-MPL's improved water-retaining and electron transport capabilities, relatively less ohmic resistances, specifically under partially humidified conditions, are observed. Even though these results are highly encouraging towards not only the manufacture of PEM fuel cells with improved performance, but also future breakthroughs, such as breaking the PEM fuel cells' dependence on external humidifiers for membrane humidification, a complete understanding of graphene-based MPL's commercial viability requires further investigations centering upon optimization and long-term performance studies.

Acknowledgements

We gratefully acknowledge the financial support of the Ontario-China Research and Innovation Fund (OCRIF Round 3) and the Natural Sciences and Engineering Research Council of Canada (NSERC) via a Discovery Grant. We would also like to express our gratitude to Group NanoXplore Inc. for supply of graphene (heXo-G V20) for the fabrication of graphene-based MPL investigated in the present study.

References

[1] Ko D, Doh S, Park HS, Kim MH. Investigation of the effect of operating pressure on the performance of proton exchange membrane fuel cell: In the aspect of water distribution. Renewable Energy; 2017. doi:10.1016/j.renene.2017.08.063.

[2] Hossain M, Islam SZ, Pollard P. Investigation of species transport in a gas diffusion layer of a polymer electrolyte membrane fuel cell through two-phase modelling. Renewable Energy 2013;51:404–18. doi:10.1016/j.renene.2012.10.008.

[3] Shin DK, Yoo JH, Kang DG, Kim MS. Effect of Cell Size in Metal Foam Inserted to the Air Channel of Polymer Electrolyte Membrane Fuel Cell for High Performance. Renewable Energy 2017. doi:10.1016/j.renene.2017.08.085.

[4] Ozden A, Alaefour IE, Shahgaldi S, Li X, Colpan CO, Hamdullahpur F. Chapter 2.28 - Gas Diffusion Layers for PEM Fuel Cells: Ex- and In-Situ Characterization, In: Exergetic, Energetic and Environmental Dimensions, 2018, pp. 695-727, https:/ /doi.org/10. 1016/B978-0-12-813734-5.00040-8.

[5] Kitahara T, Nakajima H, Inamoto M, Shinto K. Triple microporous layer coated gas diffusion layer for performance enhancement of polymer electrolyte fuel cells under both low and high humidity conditions. Journal of Power Sources 2014;248:1256–63. doi:10.1016/j.jpowsour.2013.10.066.

[6] Chen HH, Chang MH. Effect of cathode microporous layer composition on proton exchange membrane fuel cell performance under different air inlet relative humidity. Journal of Power Sources 2013;232:306–9. doi:10.1016/j.jpowsour.2013.01.079.

[7] Hunsom M, Piumsomboon P, Pruksathorn K, Tantavichet N, Endoo S, Charutavai K, Poochinda K. Novel application of Hicon Black in PEMFC microporous sublayer: Effects of composition and subsequent membrane selection. Renewable Energy 2011;36:369–73. doi:10.1016/j.renene.2010.07.002.

[8] Yan XH, Zhao TS, An L, Zhao G, Zeng L. A crack-free and super-hydrophobic cathode micro-porous layer for direct methanol fuel cells 2015;138:331–6. doi:10.1016/j.apenergy.2014.10.044.

[9] Orogbemi OM, Ingham DB, Ismail MS, Hughes KJ, Ma L, Pourkashanian M. Through-plane gas permeability of gas diffusion layers and microporous layer: Effects of carbon loading and sintering. Journal of The Energy Institute 2016. doi:10.1016/j.joei.2016.11.008.

[10] Abdelkareem MA, Tsujiguchi T, Nakagawa N. Effect of black catalyst ionomer content on the performance of passive DMFC. Journal of Power Sources 2010;195:6287–93. doi:10.1016/j.jpowsour.2010.04.070.

[11] Chun JH, Park KT, Jo DH, Lee JY, Kim SG, Park SH, Lee ES, Jyoung J, Kim SH. Development of a novel hydrophobic/hydrophilic double micro porous layer for use in a cathode gas diffusion layer in PEMFC. International Journal of Hydrogen Energy 2011;36:8422–8. doi:10.1016/j.ijhydene.2011.04.038.

[12] Artyushkova K, Pylypenko S, Dowlapalli M, Atanassov P. Structure-to-property relationships in fuel cell catalyst supports : Correlation of surface chemistry and morphology with oxidation resistance of carbon blacks. Journal of Power Sources 2012;214:303–13. doi:10.1016/j.jpowsour.2012.04.095.

[13] Lobato J, Zamora H, Cañizares P, Plaza J, Rodrigo MA. Microporous layer based on SiC for high temperature proton exchange membrane fuel cells. Journal of Power Sources 2015;288:288–95. doi:10.1016/j.jpowsour.2015.04.102.

[14] Oh H, Park J, Min K, Lee E, Jyoung JY. Effects of pore size gradient in the substrate of a gas diffusion layer on the performance of a proton exchange membrane fuel cell. Applied Energy 2015;149:186–93. doi:10.1016/j.apenergy.2015.03.072.

[15] Geim AK, Novoselov KS. The rise of graphene. Nature materials 2007;6:183-91. doi: 10.1038/nmat1849.

[16] Marinkas A, Arena F, Mitzel J, Prinz GM, Heinzel A, Peinecke V, Natter H. Graphene as catalyst support: The influences of carbon additives and catalyst preparation methods on the performance of PEM fuel cells. Carbon 2013;58:139–50. doi:10.1016/j.carbon.2013.02.043.

[17] Mu S, Chen X, Sun R, Liu X, Wu H, He D, Cheng K. Nano-size boron carbide intercalated graphene as high performance catalyst supports and electrodes for PEM fuel cells. Carbon 2016;103:449–56. doi:10.1016/j.carbon.2016.03.044.

[18] Najafabadi AT, Leeuwner MJ, Wilkinson DP, Gyenge EL. Electrochemically Produced Graphene for Microporous Layers in Fuel Cells. ChemSusChem 2016;9:1689–97. doi:10.1002/cssc.201600351.

[19] Leeuwner MJ, Wilkinson DP, Gyenge EL. Novel Graphene Foam Microporous Layers for PEM Fuel Cells: Interfacial Characteristics and Comparative Performance. Fuel Cells 2015;15:790–801. doi:10.1002/fuce.201500031.

[20] Jung G-B, Tzeng W-J, Jao T-C, Liu Y-H, Yeh C-C. Investigation of porous carbon and carbon nanotube layer for proton exchange membrane fuel cells. Applied Energy 2013;101:457–64. doi:10.1016/j.apenergy.2012.08.045.

[21] Zamel N, Li X. Effective transport properties for polymer electrolyte membrane fuel cells - With a focus on the gas diffusion layer. Progress in Energy Combustion Science 2013;39:111–46. doi:10.1016/j.pecs.2012.07.002.

[22] Ismail MS, Damjanovic T, Ingham DB, Pourkashanian M, Westwood A. Effect of polytetrafluoroethylene-treatment and microporous layer-coating on the electrical conductivity of gas diffusion layers used in proton exchange membrane fuel cells. Journal of Power Sources 2010;195:2700–8. doi:10.1016/j.jpowsour.2009.11.069.

[23] Gostick JT, Fowler MW, Pritzker MD, Ioannidis MA, Behra LM. In-plane and through-plane gas permeability of carbon fiber electrode backing layers. Journal of Power Sources 2006;162:228–38. doi:10.1016/j.jpowsour.2006.06.096.

[24] Obeisun OA, Finegan DP, Engebretsen E, Robinson JB, Taiwo OO, Hinds G, Shearing PR, Brett DJL. Ex-situ characterisation of water droplet dynamics on the surface of a fuel cell gas diffusion layer through wettability analysis and thermal characterisation. International Journal of Hydrogen Energy 2017;42:4404–14. doi:10.1016/j.ijhydene.2017.01.003.

[25] Liang H, Su H, Pollet BG, Linkov V, Pasupathi S. Membrane electrode assembly with enhanced platinum utilization for high temperature proton exchange membrane fuel cell prepared by catalyst coating membrane method. Journal of Power Sources 2014;266:107–13. doi:10.1016/j.jpowsour.2014.05.014.

[26] Han M, Xu JH, Chan SH, Jiang SP. Characterization of gas diffusion layers for PEMFC. Electrochimica Acta 2008;53:5361–7. doi:10.1016/j.electacta.2008.02.057.

[27] Abdel Hameed RM, El-Sherif RM. Microwave irradiated nickel nanoparticles on Vulcan XC-72R carbon black for methanol oxidation reaction in KOH solution. Applied Catalysis B: Environmental 2015;162:217–26. doi:10.1016/j.apcatb.2014.06.057.

[28] Marinho B, Ghislandi M, Tkalya E, Koning CE, de With G. Electrical conductivity of compacts of graphene, multi-wall carbon nanotubes, carbon black, and graphite powder. Powder Technology 2012;221:351–8. doi:10.1016/j.powtec.2012.01.024.

[29] Tseng C-J, Lo S-K. Effects of microstructure characteristics of gas diffusion layer and microporous layer on the performance of PEMFC. Energy Conversion and Management 2010;51:677–84. doi:10.1016/j.enconman.2009.11.011.

[30] Wang X, Zhang H, Zhang J, Xu H, Zhu X, Chen J, Yi B. A bi-functional micro-porous layer with composite carbon black for PEM fuel cells. Journal of Power Sources 2006;162:474–9. doi:10.1016/j.jpowsour.2006.06.064.

[31] Song S, Wang Y, Shen PK. Pulse-microwave assisted polyol synthesis of highly dispersed high loading Pt/C electrocatalyst for oxygen reduction reaction. Journal of Power Sources 2007;170:46–9. doi:10.1016/j.jpowsour.2007.04.012.

[32] Dubau L, Castanheira L, Berthomé G, Maillard F. An identical-location transmission electron microscopy study on the degradation of Pt/C nanoparticles under oxidizing, reducing and neutral atmosphere. Electrochimica Acta 2013;110:273–81. doi:10.1016/j.electacta.2013.03.184.

[33] You DJ, Kwon K, Joo SH, Kim JH, Kim JM, Pak C, Chang H. Carbon-supported ultra-high loading Pt nanoparticle catalyst by controlled overgrowth of Pt: Improvement of Pt utilization leads to enhanced direct methanol fuel cell performance. International Journal of Hydrogen Energy 2012;37:6880–5. doi:10.1016/j.ijhydene.2012.01.103.

[34] Tavakoli B, Roshandel R. The effect of fuel cell operational conditions on the water content distribution in the polymer electrolyte membrane. Renewable Energy 2011;36:3319–31. doi:10.1016/j.renene.2011.05.003.

Highlights

- Evaluated graphene as an alternative microporous layer material
- Reported morphological, structural, physical, and electrochemical characteristics
- Assessed scaled-up single cell performance of a graphene-based MPL
- Achieved highly enhanced performance under a wide range of humidity conditions